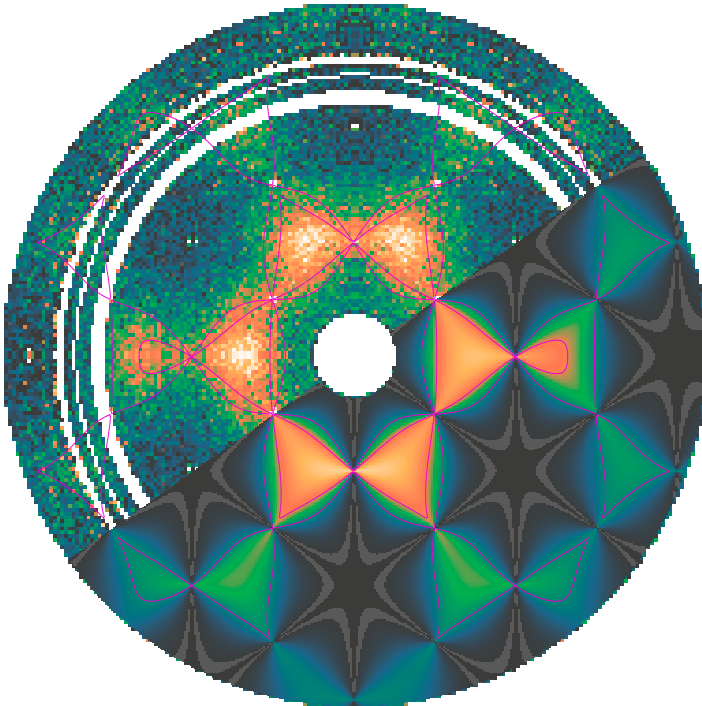
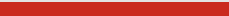


Number 54 | October 2019

SWISS NEUTRON NEWS



Schweizerische Gesellschaft für Neutronenforschung
Société Suisse de la Science Neutronique
Swiss Neutron Science Society



On the cover

Magnetic diffuse scattering in CsNiCrF₆. See the related article "Multiple Coulomb phase in the fluoride pyrochlore CsNiCrF₆" by T. Fennell et al.

Contents

- 4** The President's Page
- 6** Multiple Coulomb phase in the fluoride pyrochlore CsNiCrF_6
- 20** Advances in the high spatial resolution neutron imaging at the Paul Scherrer Institut
- 32** Announcements
- 34** Conferences and Workshops
- 39** Editorial

The President's Page

Dear fellow neutron scientists,

My first encounter with neutron science came during my studies at University of Copenhagen, where Aage Bohr taught a course exploring symmetries as underlying principles for quantum mechanics. As illustrations he used the neutron interferometry experiments pioneered by Helmut Rauch and co-workers. It was mind-bafflingly beautiful to hear how neutrons – massive particles – could be treated as wave-functions interfering with themselves across centimetre distances between ribbons of perfect silicon crystals. Later I found myself doing a PhD in neutron scattering at Risø National Laboratory, where I had the pleasure of meeting Niels Hessel Andersen, who besides his ever-enthusiastic character impressed me by running a research program from fundamental neutron studies of flux line lattices to technologically relevant development of superconducting tapes. Also during this time I had the pleasure of traveling to Warwick to do measurements in the group of Don Paul, who I enjoyed meeting over the years at facilities and meetings alike. The reason for sharing this little trip down memory lane is that within few days in September I received the sad news that these three people had passed away. I wish to dedicate this column to their honour. Neutron science is not just instruments collecting data – it is people with ideas and

collaborations. When traveling for experiments we meet colleagues who become friends. It is this facility aspect, which knits us into a community across scientific disciplines.

To finish with good news, in July this year, the Swiss membership of Institut Laue Langevin was renewed for another 5 years 2019-2023. We are grateful to the Swiss Federation and its State Secretariat for Education, Research and Innovation for supporting this important opportunity for collaborative research in disciplines from life science and engineering to fundamental quantum physics, and I look forward to meeting colleagues and friends around the instruments and coffee machines at ILL and other facilities in the coming years.

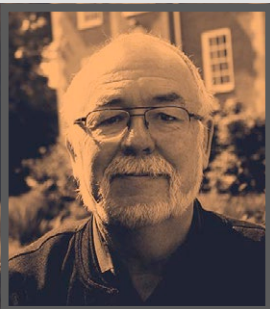
Cordially,
Henrik M. Rønnow



Helmut Rauch



Niels Hessel Andersen



Don Paul

Multiple Coulomb phase in the fluoride pyrochlore CsNiCrF_6

**T. Fennell^{1*}, M. J. Harris², S. Calder³,
M. Ruminy¹, M. Boehm⁴, P. Steffens⁴,
M.-H. Lemée-Cailleau⁴, O. Zaharko¹,
A. Cervellino⁵, S. T. Bramwell⁶**

¹Laboratory for Neutron Scattering and Imaging, Paul Scherrer Institut, 5232 Villigen PSI, Switzerland

²School of Divinity, University of Edinburgh, New College, Mound Place, Edinburgh, EH1 2LX, UK

³Quantum Condensed Matter Division, Oak Ridge National Laboratory, Oak Ridge, Tennessee 37831, USA

⁴Institut Laue-Langevin, 71 avenue des Martyrs, CS 20156, 38042 Grenoble cedex 9, France

⁵Swiss Light Source, Paul Scherrer Institut, 5232 Villigen PSI, Switzerland

⁶London Centre for Nanotechnology and Department of Physics and Astronomy, University College London, 17-19 Gordon Street, London WC1H 0AH, UK

*tom.fennell@psi.ch

After T. Fennell et al., Nature Physics 15, 60 (2019) [1]

The Coulomb phase is a state of matter in which the correlation function of local degrees of freedom can be coarse-grained and mapped to an emergent divergence-free field [2], which means that although the Coulomb phase has no broken global symmetry it has local gauge symmetry and the closed loop topology of the associated field lines. Many types of Coulomb phase are possible - including in ice and spin ice, spin liquids, dimer models, and materials with correlated structural disorder - but experimental examples other than spin ice-type magnetic systems are very scarce. Here we study the fluoride pyrochlore CsNiCrF_6 and show that this material is a multiple Coulomb phase with signature correlations in three degrees of freedom: charge configurations, atom displacements, and spin configurations.

Coulomb phases are so far identified in systems governed by a local ice rule, as is the case in all the above-mentioned examples, and illustrated in Fig. 1. The ground states of such systems have a large degeneracy and non-trivial topology, as reflected in the possible configurations of the field lines [3]; dynamics involve the formation of topological defects in the field or coherent fluctuations of the field, which can respectively be identified as generalized charges and photons of

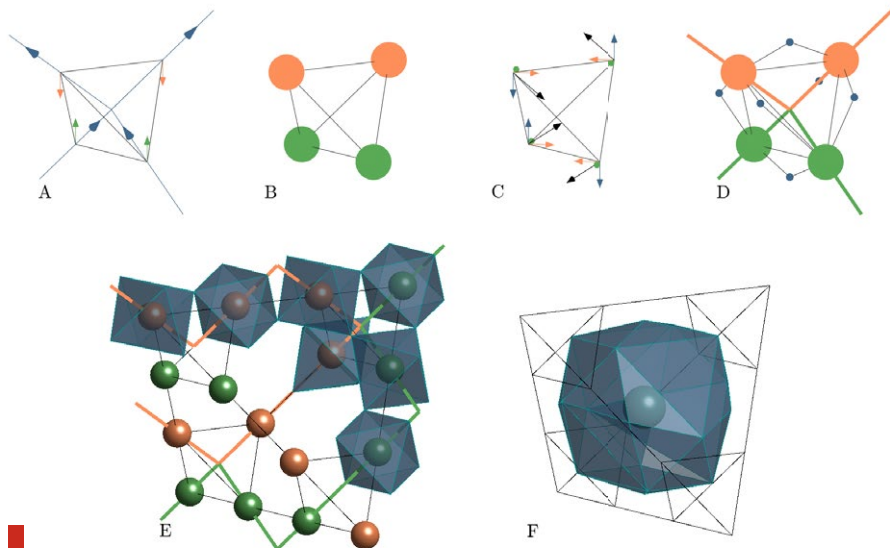


Figure 1

Illustration of Coulomb phase construction/mappings and structural features of CsNiCrF_6 .

A: The pyrochlore lattice (corner-sharing tetrahedra) supports a Coulomb phase when the local degrees of freedom can be mapped to non-divergent lattice fluxes on the diamond lattice (tetrahedron centers) [1]. The ice rule for spins in a spin ice (two-in-two-out) has a direct connection with non-divergent configurations of flux variables (blue arrows) around the diamond lattice. Antiferromagnetic pseudo-spins for a Coulomb phase when they obey a two-up-two-down rule (green and orange arrows).

B: The pseudo-spins map directly to the configurations of two cation types occupying the pyrochlore lattice and forming a charge ice (green and orange spheres).

C: When vector spins are coupled antiferromagnetically on the pyrochlore lattice (i.e. a pyrochlore Heisenberg antiferromagnet) all ground states satisfy the condition that the total magnetization of every tetrahedron is zero (e.g. black arrows). This can be ensured if the $S_{x,y,z}$ vector components are each represented by a family of pseudospins that obey the ice rule (blue, green and orange arrows).

D: The structure of CsNiCrF_6 has F^- anions (small blue spheres) coordinated to two cations (orange spheres are Cr^{3+} , green spheres are Ni^{2+}). The bond valence sums of the cations can be improved by displacing those anions shared by a pair of unlike cations towards the cation with larger charge (Cr^{3+}). The edges with non-displaced anions form a fully packed loop model on the diamond lattice (green and orange lines).

E: The structure of CsNiCrF_6 is composed of the pyrochlore lattice of cations, coordinated by octahedra of F^- ions. The octahedra share each of their vertices with another octahedron, forming tetrahedra of tilted octahedra. (Extended sections of the fully packed loop model are shown and the octahedra are drawn undistorted.)

F: The structure contains large cages in the form of an octahedron that is truncated and capped with rectangular pyramids in which the Cs^+ ions reside.

the relevant field theories [4,5,6]. This contrasts strongly with conventional phases of matter, which are characterized by a broken symmetry, local order parameter, and transverse or longitudinal fluctuations of the order parameter for excitations [7,8]. Well known Coulomb phases are classical and quantum spin ice [3,4,5,9,10,11]. In the former, the local ground state for magnetic moments has two spins pointing in and two pointing out of each tetrahedron of the pyrochlore lattice, an example of an ice rule. Connecting the tetrahedra and propagating the ice rule across the

lattice leads to power-law spin correlations, as evidenced by pinch-points in the diffuse (neutron) scattering: the signature of a Coulomb phase [2,10]. The coarse graining transformation from a spin configuration that obeys the two-in-two-out condition on every plaquette of the lattice, to a non-divergent field can be imagined qualitatively. In the classical case, dynamics are only due to the hopping of topological defects (i.e. tetrahedra where the ice rule is broken), which are the much-discussed emergent magnetic monopoles [11]. In the quantum spin ice case, co-

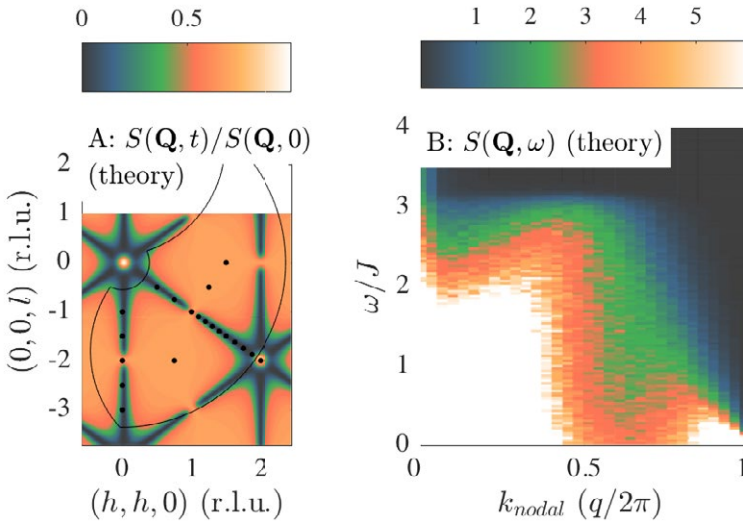


Figure 2

Theoretical predictions of the dynamics of the pyrochlore Heisenberg antiferromagnet. In large regions of reciprocal space the relaxation function $S(\mathbf{Q}, t)/S(\mathbf{Q}, 0)$ (from [18]) has identical relaxation times are expected. The scattering function at these wavevectors will have the same width, even if their (unnormalized) structure factor is different. Nodal lines joining the pinch points can be clearly seen, and different dynamical regimes are expected along these lines. Our mapping and scanning inelastic measurement positions are shown by the curved lines and dots.

B: Along a nodal line (i.e. $(h, h, -h)$) (from [17]) the spectrum shows the crossovers from gapless relaxational dynamics at the pinch point ($k_{nodal}=0$), to gapless diffusional dynamics at small $|k|$, to quasi-dispersive fast dynamics toward $|k|=0.5$, with broad and weak signal for $|k|>0.5$.

herent fluctuations of the field are also possible, and these are the sought-after emergent photons [4,5,6].

Of course, the study of Coulomb phases is also connected with the study of geometric frustration, which is a useful effect for obtaining a system with a degenerate ground state controlled by a local rule. Two historic models of frustration, the charge ice [12,13] (Fig. 1B) and the pyrochlore Heisenberg antiferromagnet [14] (Fig. 1C) are also predicted to be Coulomb phases but neither has a good experimental model system. The pyrochlore Heisenberg antiferromagnet is one of the most simply stated and canonical models of frustrated magnetism – classical spins on the pyrochlore lattice interact by a nearest neighbor antiferromagnetic interaction – and theoretical investigations show that this model exhibits all the general aspects of a Coulomb phase [14,15,16,17,18,19]. The spin correlation function has the power-law behavior, accompanied by pinch points in the static structure factor [15,19]. The continuous spins mean that a family of lattice flux fields encode ice rules for each vector spin component simultaneously, while in spin ice only one such field is required for the Ising spins. Topological defects in these flux fields are monopoles, though in this case not discrete as they are in spin ice [17,18]. Their creation or annihilation modifies the magnetic charge density locally, and relaxation of this disturbance leads to a monopole current. The associated spin relaxation rate exhibits E/T scaling and occurs at generic wave vectors, including the pinch points, as shown by the theoretical spin relaxation function $S(\mathbf{Q},t)/S(\mathbf{Q},0)$ [17,18] illustrated in Fig. 2A. Wave vectors on the nodal lines that connect the pinch points are differ-

ent to the generic points. The relaxational response at the pinch point gives way to spin diffusion at small wave vectors where fluctuations conserve the local magnetization, these are the cooperative dynamics of this type of Coulomb phase; fast, quasi-dispersive dynamics due to remnant spin waves appear further along the nodal lines, as illustrated in a cut through the simulated $S(\mathbf{Q},\omega)$ along a nodal line shown in Fig. 2B [18].

The charge ice is yet more venerable, being originally identified as an example of structural frustration by Anderson in his investigation of the magnetism and structure of ferrites (i.e. spinels in which a pyrochlore sublattice may host two different cations and/or antiferromagnetism), in which he made the connection between the configurational degeneracy of Ising-like variables on the pyrochlore lattice (be they spins or two types of cation) with that of ice [12]. The vibrational analogs of the generalized Coulomb phase dynamics described above have not been investigated, but it was recently suggested that the lattice dynamics of so-called procrystalline solids may be of interest for functional properties such as thermoelectricity [20]. A procrystalline solid is one in which the average structure is crystalline, but a disordered motif governed by a simple rule generates correlated disorder, as distinct from random or uncorrelated disorder. A charge ice would be an example of a procrystalline solid, though it is a general classification and other combinations of rules and lattices were identified. Moreover, in dense spin systems with mixed cations such as Y_2CrSbO_7 or $YbMgGaO_4$, site and bond disorder clearly have important consequences for the magnetic properties [21,22,23]. These materials are all currently suggested to have

random disorder, but although correlated disorder may be difficult to detect, it is highly probable because the long-range nature of the Coulomb interaction makes it divergent in the presence of random disorder. Further investigations of such materials may well emphasize the importance of understanding spin systems that live on structures with correlated disorder.

In this work, we used x-ray and neutron scattering to investigate correlations and dynamics in the fluoride pyrochlore CsNiCrF_6 . The structure of a fluoride pyrochlore such as CsNiCrF_6 is composed of a pyrochlore lattice occupied by the two transition metal cations. Many combinations are possible, the only requirement being that one has 2+ valence and the other 3+. The cations are coordinated by octahedra of F^- ions that share each of their vertices with another octahedron, forming tetrahedra of tilted octahedra. The structure contains large cages in which the Cs^+ ions reside, each coordinated by 18 F^- ions, giving a cage in the form of an octahedron that is truncated and capped with rectangular pyramids. These structural elements are illustrated in Fig. 1E,F. The cage centers, where the Cs^+ ions are located in the ideal structure form a diamond lattice. From the point of view of magnetism, the Curie-Weiss temperature (-70 K) suggests that in CsNiCrF_6 , the magnetic moments interact antiferromagnetically on average. CsNiCrF_6 was therefore previously suggested to be a pyrochlore Heisenberg antiferromagnet [24,25], before the concept of a Coulomb phase emerged. However, the magnetic moments have two sizes (Ni^{2+} has $S=1$, Cr^{3+} has $S=3/2$), and even under the simplest assumption different superexchange

interactions for Ni-Ni, Ni-Cr and Cr-Cr pairs should be expected. Both factors lead to the complete destruction of the local degeneracy of the true pyrochlore Heisenberg antiferromagnet that is crucial to the formation of a Coulomb phase in that model. Nonetheless, CsNiCrF_6 is highly frustrated, with significant magnetic dynamics and no order at temperatures well below the Curie-Weiss temperature pointing to a fluctuating state. With two ions of different charge on the pyrochlore lattice, it is also a candidate charge ice.

We first sought to understand the structure, tackling the average structure by conventional diffraction experiments and investigating departures from it by measuring the diffuse scattering. To investigate the average structure, we performed single crystal neutron diffraction measurements using TRICS at SINQ and VIVALDI at the ILL, and synchrotron x-ray powder diffraction experiments at the SLS. From refinement of models of the average structure against the crystallographic data we drew three conclusions: firstly, as shown in Fig. 3A, the average structure is well described by that of the mixed metal fluoride pyrochlores (see Fig. 1D,E), with isotropic displacement parameters [26]; secondly, the thermal displacement factor of the Cs^+ ion is by far the largest of all the atoms, and is strongly thermally activated as shown in Fig. 3B; lastly, split site models in which ions partially occupy a lower symmetry site around the expected position, as they do in other pyrochlore materials with structural disorder [27], are not stable or do not improve the refinements.

Because there is significant contrast in neutron scattering length between the two cations (for Ni $b_c=10.3$ fm and for Cr $b_c=3.6$

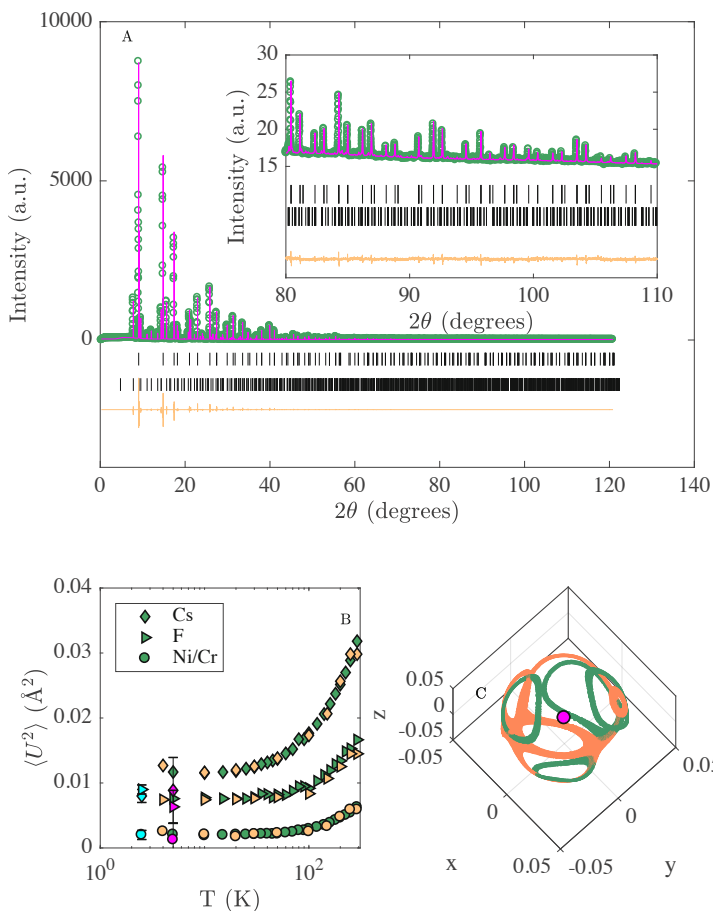


Figure 3

Average structure refinement and model parameters of CsNiCrF_6 .

A: Rietveld refinement against synchrotron x-ray powder diffraction data shows that the average structure is well described by the ideal fluoride pyrochlore structure.

B: The atomic displacement parameters as a function of temperature (at low temperature there is general agreement between two single crystal neutron diffraction experiments (cyan and magenta) performed on small pieces of one sample and the x-ray experiment performed on crushed pieces of two different samples), showing that the Cs^+ ions have the largest displacement parameters.

C: Loci of bond valence sum optimizing positions for the Cs^+ ions in two different cages of a simulation supercell. There are many possible ice rule obeying cation configurations around the cage, and hence many displacement patterns for the F^- ions that form the cage. Adding up the loci for all Cs^+ atoms in a large simulation generates a hollow spherical shell around the ideal Cs^+ position (magenta sphere at the center).

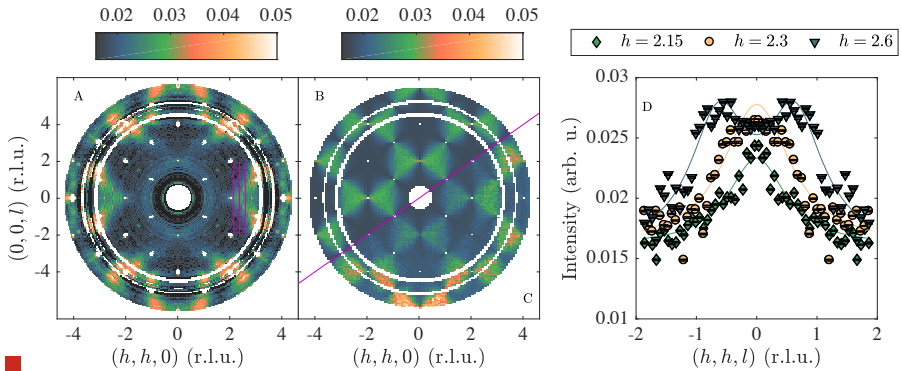


Figure 3

Structural diffuse scattering in CsNiCrF_6 .

A: Structural diffuse neutron scattering measured at 1.5 K and separated from magnetic scattering by polarization analysis (note that the colour scale starts at 0.01 (arbitrary units) to highlight the weak diffuse scattering around $(1,1,1)$ and $(0,0,2)$, there is a significant wavevector independent diffuse.

B: Predicted diffuse scattering of a charge ice with substitutional correlations only.

C: Diffuse scattering calculated for our model with charge ice cation correlations and F^- and Cs^+ displacements. In B and C the calculated intensity is multiplied by a scale factor and a wavevector independent contribution added.

D: Cuts through the experimental data (positions indicated by lines on A) show that the feature around $(h,h,0)$ sharpens inward toward the $(2,2,0)$ position, and is, therefore, the pinch point visible at that position in B and C.

fm) there should be a direct signature of charge ice correlations in the structural (i.e. nuclear) diffuse neutron scattering. The structural diffuse scattering is shown in Fig. 4A, and its form indicates that non-trivial structural correlations are indeed present. A simple model, with just the configurational correlated disorder of the cations in the charge ice has diffuse neutron scattering with the structure factor of the antiferromagnetic spin models to which it is closely connected, and the form factor for coherent nuclear scattering (i.e. essentially independent of wave vector), as in Fig. 4B, and therefore overlapping with any diffuse magnetic scattering. We therefore

used polarized neutron scattering to separate the structural and magnetic diffuse scattering, employing D7 at the ILL. However, in the experimental data the intensity of the diffuse features generally increases with the magnitude of the wavevector, as compared to the simple charge ice with diffuse features that have similar weight across the whole pattern. A Coulomb phase on the pyrochlore lattice must have pinch points at $(-2,-2,0)$ and $(0,0,2)$ [1] and these can be seen clearly in the calculation. One of these pinch points can also be seen in the experimental data, where a triangular region of intensity around $(h,h,0)$ sharpens to a point at $(2,2,0)$. The sharpening of

the scattering towards the (2,2,0) Bragg point is confirmed by cuts through the experimental data (Fig. 3D), so this feature is therefore a type of pinch point. The intense diffuse scattering around (0,0,6) at the limit of our wave vector coverage suggests another pinch point, in agreement with the calculation. The pinch points show that the ice rules have long-range coherence, and their presence in the experimental data shows unambiguously that a structural Coulomb phase is present. The other, more diffuse, features characterize local structures that exist within the Coulomb phase and show that the structure contains contributions beyond purely ice-rule obeying cation configurations. Which is to say the ice rule is obeyed, but other motifs have a greater weight in the configurations than would be expected from the ice rules alone (an example would be states formed only from hexagonal loops on the pyrochlore lattice, which obey the ice rules but whose correlation function is shorter ranged than the power-law expected for unbiased ice rules).

When working with single crystal diffuse scattering data with relatively limited wave vector access, numerical modelling in direct space is convenient [28,29,30,31,32], and we propose a simple model for our structural observations. The average structure is an efficient compromise but is frustrated: no cation has an exactly optimal bond valence sum [33], though none are far from their optimal values. Assuming perfect ice rule cation correlations amongst Ni^{2+} and Cr^{3+} across the whole lattice, we can make a local distortion throughout the structure (Fig. 1D) that optimizes the bond valence sum of both cations. The Ni/Cr cations all share four F^- with cations of the other type and two with cations of the same type. We

assume only that any F^- shared between a Ni^{2+} - Cr^{3+} pair is displaced (always by the same amount) toward the Cr^{3+} , sufficient to simultaneously optimize the bond valence sum of all Ni^{2+} and Cr^{3+} ions. Every tetrahedron therefore has four edges with a displacement and two without, a condition that can readily be represented by an ice rule on a single tetrahedron, but the relationship between ice rule and fluxes requires a sign change in 'up' and 'down' tetrahedra, since anions are displaced toward a cation in both of the tetrahedra of which the cation is a member. The required displacement is small enough to lie within the radius of the isotropic displacement parameters obtained from the diffraction data, consistent with the absence of a split site in structural refinements or Fourier difference maps. Then, if we search for the locus of sites around the ideal position that optimize the bond valence sum for each Cs^+ , we find it takes the form of one or more connected loops on the surface of a sphere, with the average over all Cs^+ sites making a hollow spherical shell (see Fig. 3C). In the average structure, with no F^- displacements, the Cs^+ bond valence sum would be optimized in four discrete pockets slightly displaced along the diamond lattice bond directions of the Cs^+ sublattice. This modification of the Cs^+ displacement from split site to hollow shell is an important aspect of the model, since the large, isotropic displacement parameter of the heaviest atom in the structure is a surprising observation. As in other cases of a hollow shell distribution, the radius of the shell is larger than the displacement parameter of the atom in the average structure [34]. The introduction of the cation correlations and local distortion of the octahedra has a strong effect on the calcu-

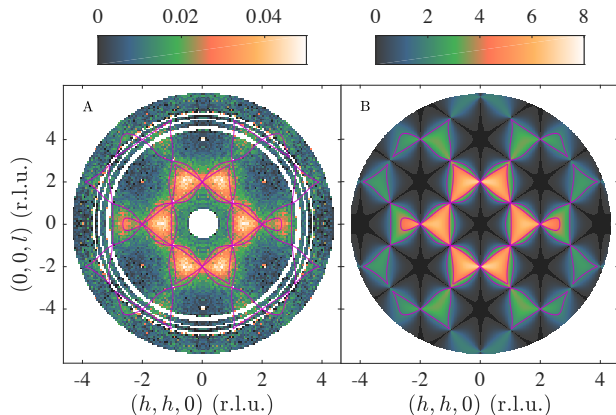


Figure 5

Magnetic diffuse scattering in CsNiCrF_6 .

A: The experimental magnetic diffuse neutron scattering measured at 1.5 K, simultaneously with the structural diffuse scattering in 4A.

B: The structure factor of the pyrochlore Heisenberg antiferromagnet (at $T=0$) including the average magnetic form factor for Ni^{2+} and Cr^{3+} [19]. Isointensity contours from the calculation are superimposed on the experimental data as guides to the eye.

lated structural diffuse scattering - the local distortions redistribute the weight towards larger wave vector, suppressing the part in the center of the pattern (Fig. 3C) but leaving the pinch point at $(2,2,0)$ described above. If the framework cations are random, the local distortions can still improve the bond valence sums, and still have the same effect on the Cs^+ displacement topology, but the diffuse scattering is a featureless response from the random cations weighted to larger wave vectors due to the displacements. Our model does not reproduce every aspect of the structural diffuse scattering pattern, but the form of the experimental data and improvements made over the simple charge ice calculation suggest the basic ingredients – a charge ice of Ni^{2+} and Cr^{3+} , displacements of the F^- anions that inherit Coulomb phase correlations from the underlying charge ice, and Cs^+ ions disordered over the surface of a spherical shell around the cage centers – are correct. The model is very simple (some additional considerations can be found in the supplementary information of [1]) and we expect to improve it by measuring structural diffuse scattering at larger wave vectors.

The Coulomb phase in the anion displacements can also be identified as a fully packed loop model. Those edges with a non-displaced F^- anion (or matching cations at each end) select two of the links of the diamond lattice that terminate at the lattice point at the center of the tetrahedron (Fig. 1D), and each of these cations is a member of another such pair on adjacent tetrahedra, similarly selecting two more diamond lattice links on these tetrahedra (Fig. 1D, E). Following the links selected in this way reveals loop in the lattice, and since every link of the diamond lattice is a member of just one loop and each diamond lattice point is visited by precisely two loops, this is an example of a fully packed loop model. The same fully packed loop model is found in a spin ice [35]. Fully packed loop models represent an intriguing type of correlated disorder, which has so far found experimental relevance only in two dimensions [36,37]. In CsNiCrF_6 , this displacement ice must play an important role in the exchange interactions and their disorder. The ideal pyrochlore Heisenberg antiferromagnet has a

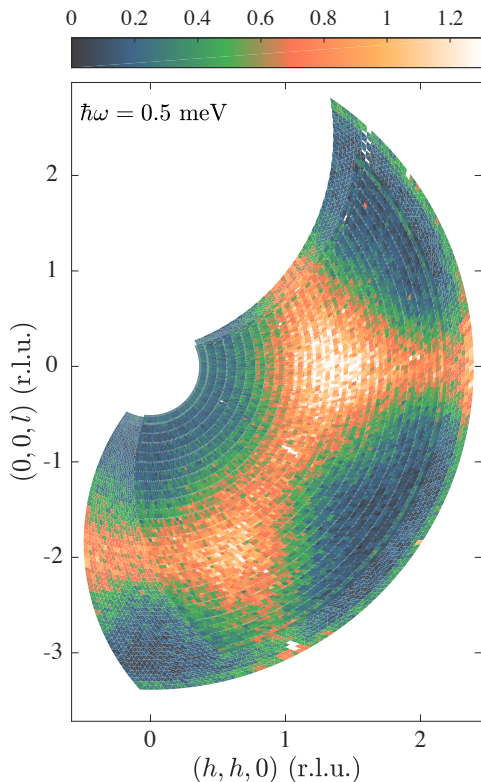


Figure 6

Wave vector dependence of magnetic dynamics in CsNiCrF_6 . $S(\mathbf{Q}, \omega)$ at 0.5 meV shows a structure factor very similar to the correlations shown in Fig. 5, but with broadened pinch points. Constant wave vector scans at pinch points and points on the structure factor where relaxational dynamics are expected (see Fig. 2) all have the same width (shown in [1]); constant wave vector scans along the nodal line $(h, h, -h)$ show a gapless spectrum at small $|\mathbf{k}|$, followed by an upward dispersive peak for $0.2 < |\mathbf{k}| < 0.5$, followed by broad, weak signals of decreasing intensity (shown in [1]). These findings are in qualitative agreement with predictions for an antiferromagnetic Coulomb phase such as the pyrochlore Heisenberg antiferromagnet.

single exchange parameter, but here we can expect three, one each for Ni-Ni, Ni-Cr and Cr-Cr bonds. The required theory will not be one of random disorder of exchange strengths, but of a strongly correlated spatial distribution of exchanges, whose structure is encoded by the fully packed loop model [38].

The magnetic diffuse scattering, obtained simultaneously in the polarized neutron scattering experiment, shows that the spins also form a magnetic Coulomb phase. The static magnetic correlations contain pinch points, distributed as in the pyrochlore Heisenberg antiferromagnet, as shown in Fig. 5A and B. The inelastic spectral weight that was previously reported was found to have a related

intensity distribution, as shown in Fig. 6, as measured using the FlatCone analyzer at IN14. Conventional TAS measurements, also using IN14, show that the dynamics have some characteristics in common with the theoretical findings for the pyrochlore Heisenberg antiferromagnet described above. At generic points on the structure factor, although the intensity may be different, the fluctuations all have the form of a quasielastic Lorentzian with the same width, as implied by the normalized correlation function shown in Fig. 2A. Along two nodal lines we measured a broad, dispersive envelope, periodic with respect to the pinch points and vanishing beyond the maximum of the dispersion, as in the calculation shown in Fig. 2B. A more detailed study would be required to examine the scaling collapse for spin diffusion at small reduced wavevector on the nodal line. These measurements are presented in Ref. 1, the point we wish to un-

derline here is that the magnetic Coulomb phase in CsNiCrF_6 has dynamics similar to those of the pyrochlore Heisenberg antiferromagnet, despite the significant differences in the underlying pattern of exchanges that we have been describing.

In Ref. [38] a model of classical spins of two types with exchange interactions distributed according to the fully packed loop model on the pyrochlore lattice was investigated by analytical calculations and numerical simulations. Four phases were identified, depending on the relative strengths of the like- and unlike-pair interactions. In the case that the interactions between the two types of like-cation pairs dominate over the interactions between the unlike pairs, a magnetic Coulomb phase is formed (phase IV of [38], two of the other phases are related ordered structures, and the last is partially ordered). The strong like-pair interactions on the fully packed loop model mean that the spins within loops, which are of the same type, are correlated antiferromagnetically, while the weaker unlike-pair interactions mean that the loops become independent of each other. The spin correlation function has the same power-law form as the pyrochlore Heisenberg antiferromagnet, with the same pattern of pinch points, but these correlations are inherited from the underlying cation or exchange structure. Our observation of the magnetic Coulomb phase in CsNiCrF_6 suggests that its exchange parameters are compatible with the magnetic Coulomb phase described in Ref [38]. It was suggested that the observation of magnetic correlations of this form in candidate materials for this model would itself signify the presence of the underlying charge ice, though we have

presented independent structural evidence that this is the case.

The theoretical dynamics of the magnetic charge ice have not been investigated in detail. In [38] they were suggested to involve spin waves living on the fully packed loops. Our observations are compatible with this, in the sense that we observe a broad dispersive envelope along the nodal line, which was associated with a remnant spin wave excitation of the highly correlated PHAFM Coulomb phase in Ref. [17]; and sharp, propagating spin wave modes would not be more probable for the magnetic Coulomb phase of Ref. [38]. However, the similarity of the dynamics that we have observed in CsNiCrF_6 with the detailed predictions of Ref. [17] suggest that the general nature and universality of Coulomb phases holds true: because both the pyrochlore Heisenberg antiferromagnet and the magnetic charge ice have similar conserved or topological quantities built from local constraints operating on the spins and leading to identical long-range parts of the correlation functions, the resulting dynamics are similar, irrespective of how these constraints are actually established. The expected clear departure from the classical pyrochlore Heisenberg antiferromagnet behavior eventually manifested in the temperature dependence of the relaxation rate at the generic wavevectors. Although this quantity is predicted to be simply proportional to the temperature and vanish as $T \rightarrow 0$ [17,18], we find a much weaker temperature dependence and residual response at the lowest temperature. Below $T=2.3$ K magnetization measurements on CsNiCrF_6 exhibit a FC/ZFC splitting similar to canonical spin glasses [24,24]. A slowing component of dynamics that coexists with the

processes we measure here, and which falls into the time window of a magnetization experiment seems by no means inconsistent with Ref. [24], but the significant inelastic spectral weight that we observe both above and far below this temperature precludes that CsNiCrF_6 is a canonical spin glass [24,24]. Given the relatively small spin sizes, the lowest temperature response may indicate that a quantum spin liquid [39] replaces the classical one.

We have found multiple Coulomb phases in CsNiCrF_6 – a charge ice and associated displacement ice, and a magnetic Coulomb phase with antiferromagnetic character. The magnetic Coulomb phase shows dynamical signatures of the pyrochlore Heisenberg antiferromagnet, a classical spin liquid of much higher local symmetry. Our results suggest that despite two systems having quite different interaction schemes, they may share many of the same physical properties, since these are controlled by the robust local gauge symmetry of the Coulomb phase and its associated conservation laws. The detailed predictions of wave vector-dependent dynamics of a classical antiferromagnetic Coulomb phase have not previously been examined experimentally, due to the absence of a good experimental model (although recent work suggests a quantum analogue in $\text{NaCaNi}_2\text{F}_7$ [40]). The consequences of ice-rules disorder in the vibrational dynamics (of the framework) have not been examined experimentally or theoretically, and this will be an interesting topic for the future. On the other hand, the interplay of framework and caged-atom dynamics are of great interest in controlling the advantageous thermoelectric properties of skutterudite and clathrate compounds such as CeF -

e_4Sb_{12} [41], and superconductivity in the analogously structured osmate pyrochlores such as KOs_2O_6 [42]. While not necessarily connected with the Coulomb phases, this represents a more general and interesting physics that can also be studied in these materials. The fluoride pyrochlore crystal structure has great chemical flexibility, including the possibilities of significantly varying the magnetic properties with numerous combinations of transition metal cations, replacing the alkali metal cation with a guest of quite different character such as NH_4^+ , or extracting it, as in FeF_3 , and of exploring charge ordered versions using compositions such as AFe_2F_6 [43,44], perhaps with a view to metallization. We therefore suggest that these compounds are of considerable interest for exploration of both unconventional spin correlations and dynamics (and the phases of [38]), as well as new functionalities based on correlated disorder.

- [1] T. Fennell, M. J. Harris, S. Calder, M. Ruminy, M. Boehm, P. Steffens, M.-H. Lemée-Cailleau, O. Zaharko, A. Cervellino, S. T. Bramwell, Multiple Coulomb phase in the fluoride pyrochlore CsNiCrF₆. *Nature Physics* **15**, 60 (2019)
- [2] C. L. Henley, The “Coulomb phase” in frustrated systems. *Annual Review of Condensed Matter Physics* **1**, 179–210 (2010).
- [3] L. D. C. Jaubert, M. J. Harris, T. Fennell, R. G. Melko, S. T. Bramwell, P. C. W. Holdsworth, Topological-Sector Fluctuations and Curie-Law Crossover in Spin Ice. *Physical Review X* **3**, 011014 (2013).
- [4] M. Hermele, M. P. A. Fisher, L. Balents, Pyrochlore photons: The U(1) spin liquid in a S=1/2 three-dimensional frustrated magnet, *Physical Review B* **69**, 064404 (2004).
- [5] O. Benton, O. Sikora, N. Shannon, Seeing the light: Experimental signatures of emergent electromagnetism in a quantum spin ice. *Physical Review B* **86**, 075154 (2012).
- [6] M. J. P. Gingras, P. A. McClarty, Quantum spin ice: a search for gapless quantum spin liquids in pyrochlore magnets. *Reports on Progress in Physics* **77**, 056501 (2014).
- [7] L. D. Landau, E. M. Lifshitz, *Statistical Physics* (Pergamon, New York, 1980).
- [8] D. Pekker, C. M. Varma, Amplitude/Higgs Modes in Condensed Matter Physics. *Annual Review of Condensed Matter Physics*, **6**, 269–297 (2015).
- [9] M. J. Harris, S. T. Bramwell, D. F. McMorrow, T. Zeiske, K. W. Godfrey, Geometrical Frustration in the Ferromagnetic Pyrochlore Ho₂Ti₂O₇. *Physical Review Letters* **79**, 2554–2557 (1997).
- [10] T. Fennell, P. P. Deen, A. R. Wildes, K. Schmalzl, D. Prabhakaran, A. T. Boothroyd, R. J. Aldus, D. F. McMorrow, S. T. Bramwell, Magnetic Coulomb Phase in the Spin Ice Ho₂Ti₂O₇. *Science* **326**, 415–417 (2009).
- [11] C. Castelnovo, R. Moessner, S. L. Sondhi, Magnetic monopoles in spin ice. *Nature* **451**, 42–45 (2008).
- [12] P. W. Anderson, Ordering and antiferromagnetism in ferrites. *Physical Review* **102**, 1008–1013 (1956).
- [13] P. A. McClarty, A. O'Brien, F. Pollmann, Coulombic charge ice. *Physical Review B* **89**, 195123 (2014).
- [14] R. Moessner, J. T. Chalker, Properties of a classical spin liquid: The Heisenberg pyrochlore antiferromagnet, *Physical Review Letters* **80**, 2929–2932 (1998).
- [15] S. V. Isakov, K. Gregor, R. Moessner, S. L. Sondhi, Dipolar spin correlations in classical pyrochlore magnets. *Physical Review Letters* **93**, 167204 (2004).
- [16] R. Moessner, J. T. Chalker, Low-temperature properties of classical geometrically frustrated antiferromagnets. *Physical Review B* **58**, 12049–12062 (1998).
- [17] P. H. Conlon, J. T. Chalker, Spin Dynamics in Pyrochlore Heisenberg Antiferromagnets. *Physical Review Letters* **102**, 237206 (2009).
- [18] P. H. Conlon, “Aspects of Frustrated Magnetism”, thesis, Oxford University, Oxford (2010).
- [19] C. L. Henley, Power-law spin correlations in pyrochlore antiferromagnets. *Physical Review B* **71**, 014424 (2005).
- [20] A. R. Overy, A. B. Cairns, M. J. Cliffe, A. Simonov, M. G. Tucker, A. L. Goodwin, Design of crystal-like aperiodic solids with selective disorder–phonon coupling. *Nature Communications* **7**, 10445 (2016).
- [21] L. Shen, C. Greaves, R. Riyat, T. C. Hansen, and E. Blackburn, Absence of magnetic long-range order in Y₂CrSbO₇: Bond-disorder-induced magnetic frustration in a ferromagnetic pyrochlore, *Physical Review B* **96**, 094438 (2017).
- [22] Y. Li, D. Adroja, R. I. Bewley, D. Voneshen, A. A. Tsirlin, P. Gegenwart, and Q. Zhang, Crystalline Electric-Field Randomness in the Triangular Lattice Spin-Liquid YbMgGaO₄, *Physical Review Letters* **118**, 107202 (2017).
- [23] Z. Zhu, P. A. Maksimov, S. R. White, and A. L. Chernyshev, Disorder-Induced Mimicry of a Spin Liquid in YbMgGaO₄, *Physical Review Letters* **119**, 157201 (2017).
- [24] M. J. Harris, M. P. Zinkin, T. Zeiske, Magnetic excitations in a highly frustrated pyrochlore antiferromagnet. *Physical Review B* **52**, R707–R710 (1995).
- [25] M. P. Zinkin, M. J. Harris, T. Zeiske, Short-range magnetic order in the frustrated pyrochlore antiferromagnet CsNiCrF₆. *Physical Review B* **56**, 11786–11790 (1997).
- [26] D. Babel, G. Pausewang, W. Viebahn, Die Struktur einiger Fluoride, Oxide und Oxidfluoride AMe₂X₆ der RbNiCrF₆-Typ. *Zeitschrift fuer Naturforschung, Teil B. Anorganische Chemie, Organische Chemie* **22**, 1219-1220 (1967).

- [27] D. P. Shoemaker, R. Seshadri, A. L. Hector, A. Llobet, T. Proffen, C. J. Fennie, Atomic displacements in the charge ice pyrochlore $\text{Bi}_2\text{Ti}_2\text{O}_6\text{O}'$ studied by neutron total scattering. *Physical Review B* **81**, 144113 (2010).
- [28] D. A. Keen, A. L. Goodwin, The crystallography of correlated disorder. *Nature* **521**, 303–309 (2015).
- [29] T. R. Welberry, B. D. Butler, Interpretation of diffuse X-ray scattering via models of disorder. *Journal of Applied Crystallography* **27**, 205–231 (1994).
- [30] R. B. Neder, T. Proffen, “Diffuse Scattering and Defect Structure Simulations: A cook book using the program DISCUS” (Oxford University Press, Oxford, 2008).
- [31] J. A. M. Paddison, A. L. Goodwin, Empirical Magnetic Structure Solution of Frustrated Spin Systems. *Physical Review Letters* **108**, 017204 (2012).
- [32] S. J. L. Billinge, I. Levin, The Problem with Determining Atomic Structure at the Nanoscale. *Science* **316**, 561–565 (2007).
- [33] I. D. Brown, Recent Developments in the Methods and Applications of the Bond Valence Model. *Chemical Reviews* **109**, 6858–6919 (2009).
- [34] V. V. Chernyshev, S. G. Zhukov, A. V. Yatsenko, L. A. Aslanov, and H. Schenk, The use of Continuous Atomic Distributions in Structural Investigations. *Acta Crystallographica Section A: Foundations of Crystallography* **50**, 601–605 (1994).
- [35] L. D. C. Jaubert, M. Haque, R. Moessner, Analysis of a Fully Packed Loop Model Arising in a Magnetic Coulomb Phase, *Physical Review Letters* **107**, 177202 (2011).
- [36] M. O. Blunt, and J. C. Russell, M. D. C. Giménez-López, J. P. Garrahan, X. Lin, M. Schröder, N. R. Champness, P. H. Beton, Random Tiling and Topological Defects in a Two-Dimensional Molecular Network, *Science* **322**, 1077–1081 (2008).
- [37] J. L. Jacobsen, F. Alet, Semiflexible Fully Packed Loop Model and Interacting Rhombus Tilings, *Physical Review Letters* **102**, 145702 (2009).
- [38] S. T. Banks, S. T. Bramwell, Magnetic frustration in the context of pseudo-dipolar ionic disorder. *EPL (Europhysics Letters)* **97**, 27005 (2012).
- [39] L. Savary, L. Balents, Quantum spin liquids: a review. *Reports on Progress in Physics* **80**, 016502 (2016).
- [40] K. W. Plumb, J. Hirtesh, J. Changlani, A. Scheie, Shu Zhang, J. W. Kriza, J. A. Rodríguez-Rivera, Yiming Qui, B. Winn, R. J. Cava, C. L. Broholm, Continuum of quantum fluctuations in a three-dimensional $S=1$ Heisenberg magnet. *Nature Physics* **15**, 54 (2019).
- [41] M. M. Koza, M. R. Johnson, R. Viennois, H. Mutka, L. Girard, D. Ravot, Breakdown of phonon glass paradigm in La- and Ce-filled $\text{Fe}_4\text{Sb}_{12}$ skutterudites. *Nature Materials* **7**, 805–810 (2008).
- [42] T. Shimojima, Y. Shibata, K. Ishizaka, T. Kiss, A. Chainani, T. Yokoya, T. Togashi, X.-Y. Wang, C. T. Chen, S. Watanabe, J. Yamaura, S. Yonezawa, Y. Muraoka, Z. Hiroi, T. Saitoh, S. Shin, Interplay of Superconductivity and Rattling Phenomena in β -Pyrochlore KOs_2O_6 Studied by Photoemission Spectroscopy. *Physical Review Letters* **99**, 117003 (2007).
- [43] R. De Pape, G. Ferey, A new form of FeF_3 with the pyrochlore structure: Soft chemistry synthesis, crystal structure, thermal transitions and structural correlations with the other forms of FeF_3 . *Materials Research Bulletin* **21**, 971–978 (1986).
- [44] S. W. Kim, S.-H. Kim, P. S. Halasyamani, M. A. Green, K. P. Bhatti, C. Leighton, H. Das, C. J. Fennie, $\text{Rb-Fe}^{2+}\text{Fe}^{3+}\text{F}_6$: Synthesis, structure, and characterization of a new charge-ordered magnetically frustrated pyrochlore-related mixed-metal fluoride. *Chemical Science* **3**, 741–751 (2012).

Advances in the high spatial resolution neutron imaging at the Paul Scherrer Institut

P. Trtik, E.H. Lehmann, M. Strobl,
M. Meyer, T. Wehmann

Paul Scherrer Institut (PSI),
5232 Villigen PSI, Switzerland

1. Introduction

Neutron imaging as an experimental method complementary to that of other transmission imaging techniques (e.g. that of X-rays imaging) has long¹ been utilized for a broad spectrum of scientific questioning. While the early neutron radiographies were based on the neutron converters combined with film, a quantum step in neutron imaging achieved by the introduction of digital neutron imaging (predominantly using neutron sensitive scintillator screens and charge coupled devices) in the early 1990s allowed for acquisitions of series of time-resolved neutron radiographies and neutron tomographies.

The evaluation of the neutron transmission imaging is based on Beer-Lambert law,

$$\frac{I_{out}}{I_{in}} = e^{-\Sigma(x,y) \cdot s(x,y)}$$

where $\Sigma(x,y)$ is the total linear attenuation coefficient of the transmitted material in pixel position (x,y) and $s(x,y)$ is the path length of the transmitted neutrons through the sample in pixel position (x,y) .

The local object transmittance at position (x,y) is obtained through pixel-wise referencing of the sample image $I(x,y)$ with an open beam image $I_o(x,y)$ (i.e. the image acquired without any sample) and a dark current image

$I_D(x, y)$ (i.e. image acquired without neutron illumination) using the Eq. 2:

$$T(x, y) = \frac{I_{out}}{I_{in}} = \frac{I(x, y) - I_D(x, y)}{I_0(x, y) - I_D(x, y)}$$

The achievable spatial resolution is a key quality factor for any imaging method. Limitations to the spatial resolution provided by neutron imaging are implied by three main factors. Firstly, the neutron detection process involves intermediate particles (the conversion electrons in the case Gd-based detection and alpha and triton in the case of Li-based detection) whose mean free path length in the detection material contributes to the resulting image blur. The second reason is connected to the divergence of the neutron beam utilized for imaging. The divergence (usually expressed by the so-called L/D ratio of the utilized pinhole geometry for imaging, where D is the diameter of the beam defining aperture and L is its distance between such aperture and the sample position) leads to higher image blur for objects positioned further away from the imaging detector. Third, even though the available neutron flux is not directly affecting the intrinsic spatial resolution of neutron imaging detectors, it is in all practical terms limiting the spatial resolution of neutron transmission imaging that can be achieved in a reasonable experimental time².

There are therefore competing requirements on the optimization of the scintillator-based neutron imaging detectors. While thinner scintillator screens provide higher spatial resolutions, the detection efficiency intrinsically decreases with the screen thickness. The original digital neutron imaging has been performed using ⁶LiF/ZnS scintillator screens^{3,4}. Being bicomponent material

(⁶LiF – the neutron absorber, ZnS – the light emitter) of relatively low neutron capture efficiency, the ⁶LiF/ZnS screens are usually utilized in thicknesses larger than 100 μm and the spatial resolution is therefore correspondingly limited to similar values. Higher resolutions ($\sim 30 \mu\text{m}$) could have been later achieved by detectors using gadolinium oxysulfide screens^{5,6} that are usually used in thickness of 10 to 20 micrometers. Thinner scintillators based on natural gadolinium oxysulfide exhibit rather low neutron detection efficiency⁷. Higher spatial resolutions ($\sim 10 \mu\text{m}$) -albeit in one image direction only- were achieved using tilted scintillator-based detectors and proved useful for imaging of fuel cells⁸. Further progress has been achieved in recent years at the Paul Scherrer Institut (PSI) within the framework of ‘PSI Neutron Microscope’ project in which the scintillator screens based on isotopically enriched 157-gadolinium were developed.

The aim of this article is to focus on this particular advancement and to underline its significance with examples of several applications that were enabled by the availability of the very high spatial resolution neutron imaging. Last but not the least, the paper is concluded with an outlook into the future possible avenues for further enhancements.

2. ‘PSI Neutron Microscope’

High spatial resolution neutron imaging is a fast-developing area driven by the demands from the user community. Provided that ‘high resolution neutron imaging’ is loosely defined as neutron imaging with the capability to resolve about 10 μm structures or better, there

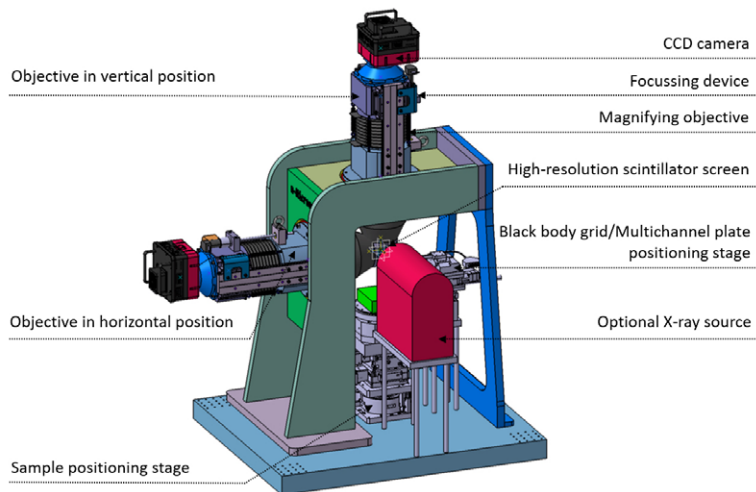


Figure 1

3D drawing of the ‘PSI Neutron Microscope’ high resolution neutron imaging detector. (Figure adapted from¹⁵ Trtik et al., 2017)

are several approaches that demonstrate such capability^{9,10,11,12,13}. At PSI, a high-resolution neutron imaging detector has been developed within the framework of the ‘Neutron Microscope’ (NM) project. As neutrons are not focussed using this device, the NM is not *per se* a neutron microscope and can be described more precisely as a ‘high resolution, high numerical aperture optical microscope with the light input based on the high performance neutron sensitive scintillators’. The NM detector has been developed in two stages. The first prototype of the detector utilized a magnifying objective with a 4 μm thick gadolinium oxysulfide ($\text{Gd}_2\text{O}_2\text{S:Tb}$) scintillator screen and has been able to acquire images of approximately 8 micrometers spatial resolution¹⁴.

In the current version of NM, a tailored objective of high numerical aperture ($\text{NA}=0.4$) composed of thirteen individual lenses (the three of which closest to the scintillator screen made of radiation hard glass) has been coupled with the isotopically-enriched 157-gadolinium oxysulfide ($^{157}\text{Gd}_2\text{O}_2\text{S:Tb}$; hereafter referred to as 157-gadox)¹⁶. The scintillator

screen represents the central aspect in the high spatial resolution detection of neutrons. The provision of highly isotopically enriched (more than 88%) gadolinium-based scintillator screens enabled to overcome the contradictory requirements of the high spatial resolution and the high detection efficiency. It was shown that both the neutron absorption power and the generated light output increased approximately by a factor of four when compared with the scintillator screens based on natural unenriched gadolinium oxysulfide. The NM has been designed as a self-contained detector (including its own dedicated sample positioning stage – see Fig.1) independent from the current operating infrastructure of the PSI neutron imaging beamlines and can therefore be transferred between various beamlines rather easily providing enough space is available at the given beamline. The

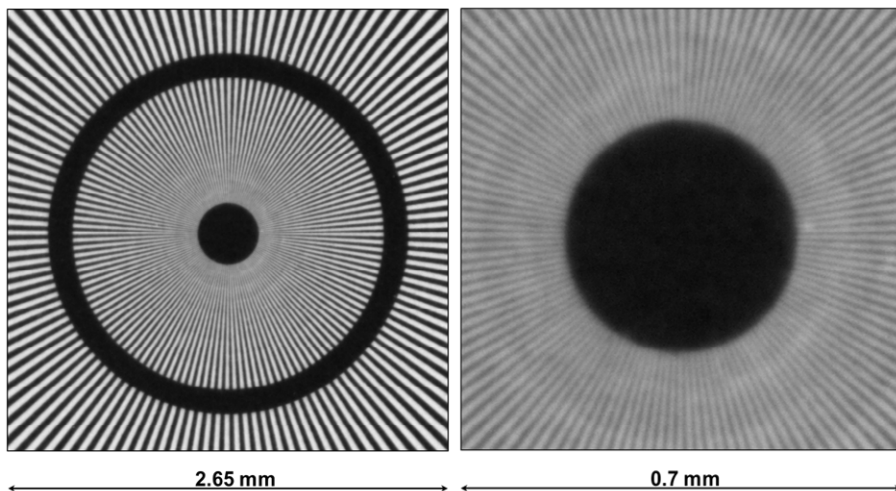


Figure 2

(left) neutron radiography of a Gd based Siemens star acquired using ‘PSI Neutron Microscope’, (right) close-up of the centre of the Siemens star of the left hand side image clearly revealing the ends of the approximately 4 micrometre spokes. (Figure adapted from¹⁹ Trtik et al., 2019)

NM can utilize various CCD/sCMOS cameras and offers routinely the pixel size of the acquired images as low as 1.3 micrometres¹⁷. The real spatial resolution of the NM detector is in sub-5 μm domain as demonstrated using the Siemens star¹⁸ test object (see Fig.2). The Fourier ring correlation assessment of the Siemens star image delivers 4.6 micrometres spatial resolution and by visual inspection the approximately 4 micrometres thin ends of the individual spokes of the test pattern can be discerned¹⁹. Further enhancement of the light output has been recently achieved by structuring the 157-gadox scintillator screen substrates²⁰.

Apart from the advances in the available spatial resolution, there has been recent progress also regarding the quantification precision of neutron imaging. An experimental

approach to compensate for scattering and systematic biases in quantitative neutron imaging – the so called black body (BB) correction – using grids of neutron opaque bodies has been recently proposed²¹ and implemented²². Unlike the case of the neutron imaging with lower resolution set-ups in which BBs based on $^{10}\text{B}_4\text{C}$ cylinders were used, the miniaturized BB grids for NM were fabricated using $^{157}\text{Gd}_2\text{O}_3$ powders. The contributions of the sample scattered neutrons and of the background can be measured locally “behind” the black bodies and subsequently estimated for the entire image.

Figure 3 shows all the raw data images that are necessary to be acquired for the neutron radiography with BB correction that allow for quantitatively correct assessment of linear

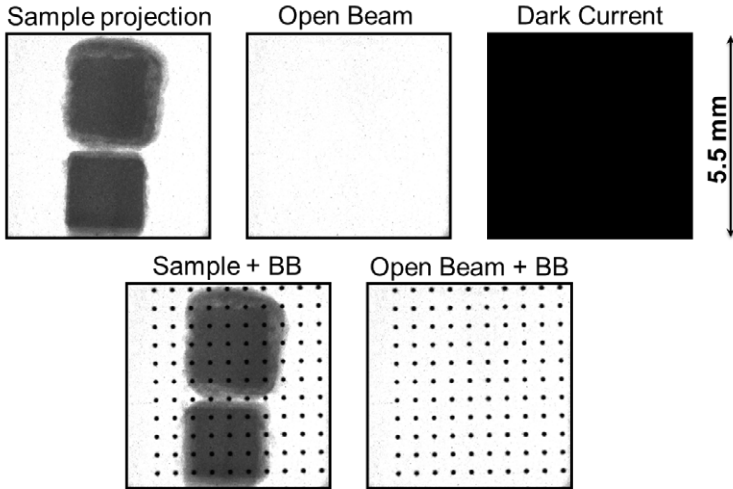


Figure 3

Set of raw images required for the black-body correction of quantitative neutron radiography.

attenuation coefficients. The BB correction has become a useful tool, in particular for the measurements in which the quantitative values of material compositions are in the focus of scientific questioning.

3. Examples of high resolution neutron imaging applications

Following on the above advances, the NM was included in the PSI standard user program as an add-on detector available at the ICON²³ and the POLDI²⁴ beamlines. Its hitherto unprecedented high spatial resolution has spurred significant interest and attracted in 2017-18 over 40 beamtime proposals (overbooking factor >1.5) from a rather broad spec-

trum of scientific disciplines. The following paragraphs will shortly present three applications for which the high resolution neutron imaging has provided information not amenable (or hardly amenable) otherwise.

3.1. Hydrogen quantification in nuclear fuel claddings

Thanks to an order of magnitude higher neutron cross-section of hydrogen than zirconium, neutron imaging provides an excellent approach for the determination of hydrogen concentrations in zirconium alloy fuel claddings. The knowledge of the distribution of hydrogen in such claddings is of utmost importance for the safety, as hydrogen (presented as the zirconium hydride) causes depreciation of its mechanical properties (embrittlement).

The improvement of spatial resolution of neutron imaging down to the scale of the common width of zirconium hydride packets

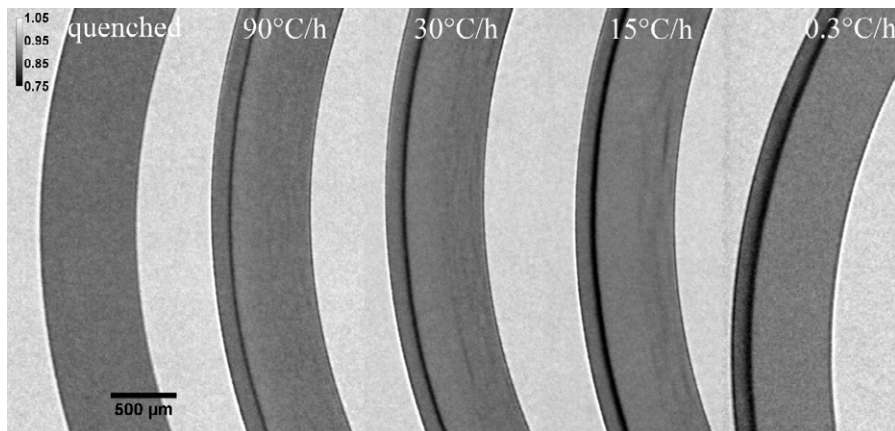


Figure 4

(left) Neutron radiographs of the duplex nuclear fuel cladding tubes (loaded with 200 wppm hydrogen) with 150 micrometres thick outer liner clearly revealing the influence of the cooling rate on the hydrogen redistribution (from²⁵ Gong et al., 2019)

enabled quantitative detection of hydrogen concentration distributions in cladding cross-sections. The recent publication²⁵ presents the investigation on the hydrogen redistribution induced by diffusion-precipitation in a 4.5 mm duplex cladding containing two composition-differed material layers (outer liner and substrate) with effective spatial resolution of 9.6 μm (see Fig.4).

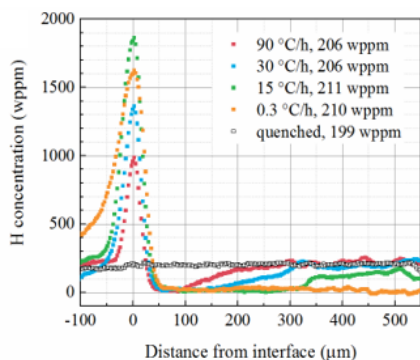


Figure 5

Quantification of the hydrogen concentration across the cladding wall thickness for the images shown in Figure 4. Zero distance is set at the liner-substrate interface (from²⁵ Gong et al., 2019).

It has been clearly demonstrated that the cooling rate has a significant influence on the hydrogen concentration across the cladding wall thickness. The distribution of hydrogen concentration across the cladding wall was detected by averaging approximately 1000 circumferential pixels over the radial direction corresponding to an approximate volume gauge of $0.0027 \times 2.7 \times 4.5 \text{ mm} \times \text{mm} \times \text{mm}$. The hydrogen concentration resolution of 9 wppm (0.08 atomic per cents) in the same image was achieved. The high spatial resolution of the NM together with its sub-10 wppm

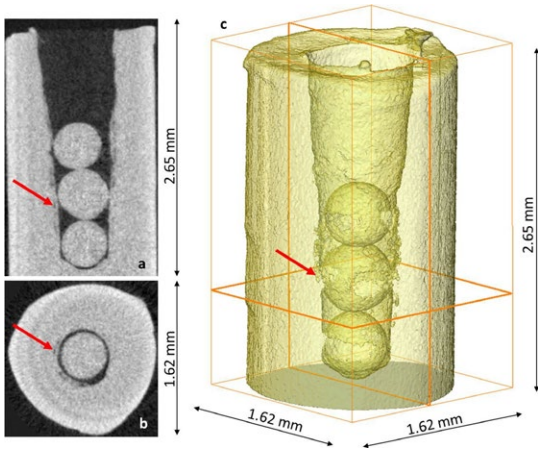


Figure 6

(a) vertical and (b) horizontal slice of the reconstructed neutron microtomographic dataset revealing porosity in the gold sample with high resolution (dataset voxel size $5.4\ \mu\text{m}$). (c) 3D partially transparent rendering of the sample clearly revealing the artificial pore space. Positions of the horizontal and vertical slices shown in Figs. 3a and 3b are indicated. The porosity occurring in the close vicinity of the drilled hole is indicated by the red arrows in all three images (from²⁶ Trtik, 2017).

sensitivity to hydrogen in zirconium alloys is currently unique and the future work will focus on the assessment of hydrogen distribution in highly activated cladding elements that were operated in (Swiss) nuclear power plants.

3.2. Porosity distribution in high-Z materials

Another domain in which neutron imaging finds interesting niche applications are the high-Z materials that are otherwise hard to be transmitted by other sources of readily available radiation (such as tabletop X-rays). Neutron cross-sections of several high-Z materials are such that they allow successful transmission imaging even for relatively thick samples. As a result, samples of such materials of $\sim\text{mm}$ to $\sim\text{cm}$ in diameter can be imaged with high resolution in 3D by neutron microtomography. As a proof-of-the-concept experiment, a model sample of gold with artificially induced pore space (a cylinder with a drilled hole filled with

several small gold spheres) was investigated²⁶ using NM at the BOA beamline²⁷ at PSI. The available neutron flux at BOA is (for the given experimental conditions) limited to $\sim 5 \times 10^6\ \text{n cm}^{-2}\ \text{s}^{-1}$. Consequently, neutron microtomography in BOA requires rather long acquisition times. However, with slightly over 2 days of acquisition time a neutron microtomographic dataset has revealed segmented porosity with $5.4\ \mu\text{m}$ voxel size and the spatial resolution close to 10 micrometres (see Fig.6). This proof-of-the-concept experiment confirmed a clear potential of neutron microtomography for investigation of porosities in high-Z materials, such as additively manufactured (AM) precious alloys.

Additive manufacturing (AM) is a relatively new fast-developing technological domain and the selective laser melting (SLM) is one of the most important additive manufacturing (AM) processes, which enables the production of very complex metallic objects from a computer-aided design file. In SLM, the struc-

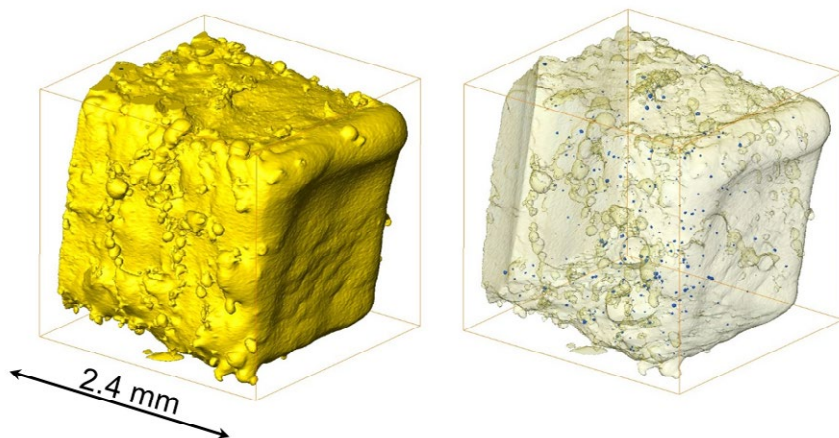


Figure 7

Neutron microtomography: (right) 3D rendering of additively manufactured gold alloy sample showing (left) the closed porosity in blue colour

ture-property relationship of the produced materials are dependent on numerous manufacturing parameters (including those of the laser scanning). One of the main criterion regarding the success of the AM process is the porosity content of the printed samples. While the pore size distribution for the majority of AM materials can be readily obtained with X-ray microtomography, the AM precious alloys are intrinsically more difficult to be transmitted by X-rays. At the same time, the information on pore size distribution by SLM printed precious metal alloys is demanded by the jewelry and watch industries.

As mentioned above, the existing neutron sources are rather flux limited for the purpose of high-resolution imaging. Consequently, the neutron microtomography with the spatial resolution in single micrometres domain is best to be performed at the highest flux neutron sources available. The NM detector has been recently installed at ILL-D50 beamline.

There, the neutron microtomography (voxel size of $2.7 \mu\text{m}$) revealed pores down to $10 \mu\text{m}$ in size in $\sim 2 \text{ mm}$ cuboid AM gold alloy samples (see Fig.7).

3.3. Visualization of cavitation in realistic Diesel injection nozzles

Apart from the materials science studies, the high resolution neutron imaging provides also an interesting option for operando investigations of working devices. The high-resolution neutron imaging has been utilized for the in-situ assessment of the cavitation inside the spray hole of operating realistic Diesel injection nozzle. A prototype of a chamber for in-situ operando Diesel injection nozzle neutron imaging has been developed and recently tested²⁸ using NM at the POLDI beamline. Different cavitation modes were observed using NM inside the realistic real-size spray

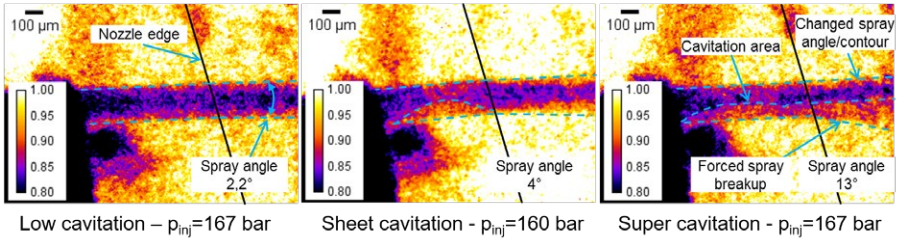


Figure 8

Neutron radiographs of operando Diesel injection nozzle showing the different cavitation modes in the spray hole and its influence on the exit spray angle. (from²⁸ Thimm et al., 2019)

hole. The cavitation modes could have been also correlated with the observed exit spray angle (see Fig 8).

While the injection nozzle used in this pilot experiment was operating under quasi-stationary pressure conditions and utilized water gadolinium salt solution as injection medium, the realistic experiments using Diesel are in preparation.

4. Discussion of outlook for future improvements

As neutron sources are flux limited in general, the focus of the future advancement of the high-resolution neutron imaging should be directed not only on the enhancement of resolution itself, but also on the detection efficiency of high resolution neutron imaging detectors. For the scintillator-based detectors, the future work towards higher efficiency is foreseen through engineering/microstructuring the high-resolution neutron sensitive powder scintillator screens and by production of low porosity ceramic scintillators²⁹ based on isotopically enriched ¹⁵⁷Gd materials. Regarding the further enhancement of spatial

resolution itself, the centroiding of single neutron events^{30,31} represents one of the viable ways for future progress, in particular when combined with the use of the extremely thin isotopically-enriched gadolinium oxysulfide scintillator screens. Parallel to that, Fourier ptychographic neutron imaging (FPNI) has been recently proposed – based on its X-ray variant³² – as a viable alternative for exceeding the resolution limits of the NM detector. In this approach, the intrinsic inhomogeneities of the gadolinium oxysulfide powder scintillators (instead of the modulation of neutron illumination itself) shall provide the modulation for the sample scanning. Both mentioned methods aim at being able to reach 1 micrometre spatial resolution. Above that, the enhancement of spatial resolution via combined use of dedicated neutron optics (such as Wolter mirrors³³) and the high resolution scintillator based neutron detectors (such as NM) will be also considered.

Based on the hitherto experience with the NM, a number of specific applications that would profit from such further enhancement in resolution, including operando imaging of fuel cell catalyst layers³⁴, and others.

5. Conclusions

The recent progress within the ‘PSI Neutron Microscope’ project at PSI has extended the spatial resolution of the neutron imaging. The developed detector pushed the available resolution to the sub-5 μm domain, thus opening avenues for new science. The examples of applications include but are not limited to the hydrogen quantification in nuclear fuel claddings, the 3D imaging of porosity in additively manufactured high-Z alloys, and the visualization of cavitation in realistic Diesel injection nozzles. Further advances of neutron imaging both on the detector efficiency and the spatial resolution side are shortly discussed.

The authors sincerely acknowledge the contributions of L. Thimm, H. Hansen, F. Dinkelacker (all Leibniz University of Hannover, Germany) and S. Jollet (PSI Villigen Switzerland) to the topic of visualization of cavitation in Diesel injection nozzles. D. Atkins, A. Tenggattini (both ILL, France) are thanked for their assistance with the experiments performed at ILL-D50 beamline.

Work presented here is based on the high resolution neutron imaging experiments using PSI Neutron Microscope detector at the BOA, ICON & POLDI, beamlines at the Swiss Spallation Neutron Source SINQ, Paul Scherrer Institut, Villigen, Switzerland and at the D50 beamline at the Institut Laue-Langevin, Grenoble, France.

Acknowledgement

The authors sincerely acknowledges the valuable contributions from the following colleagues: J. Hovind, J. Crha, C. Carminati, P. Boillat, F. Schmid, P. Vontobel, M. Morgano, M. Raventos, M. Siegwart, D. Mannes, C. Grünzweig, A. Kaestner, G. Mikuljan, J. Vila-Comamala, T. Neiger, C. David, E. Müller, A. Menzel, K. Wakonig, (all PSI Villigen Switzerland) and B. Braunecker, M. Biber (both Braunecker AG, Switzerland).

J. Bertsch, W. Gong, L. Duarte, R. Zubler, A. Colldeweih, (all PSI Villigen Switzerland) and M. Grosse (KIT, Germany) are very much thanked for their excellent contributions and scientific ideas to the topic of hydrogen quantification in nuclear fuel claddings.

H. Ghasemi, J. Jhabvala, R. Loge (all EPFL, Switzerland) are thanked for their contributions to the investigations of porosity in precious metal alloys.

- [1] Peter, O. Neutronen-Durchleuchtung. *Zeitschrift fuer Naturforsch.* 1, Neutronen-Durchleuchtung (1946).
- [2] Grosse, M. & Kardjilov, N. Which Resolution can be Achieved in Practice in Neutron Imaging Experiments? - A General View and Application on the Zr - ZrH₂ and ZrO₂- ZrN Systems. in *Physics Procedia* (2017).
- [3] Kobayashi, H; Tomura, K; Harasawa, S; Harasawa, M. Neutron radiography using cooled CCD camera. *Neutron Radiogr. - Proc. WCNR-3* 421–428 (1990).
- [4] McFarland, E; Lanza, R; Na, H; McGuire, M; Dai, H. Quantitative evaluation of a neutron radiography and tomography using cooled charged coupled devices designed for low fluence sources. *Neutron Radiogr. - Proc. WCNR-4* 561 (1992).
- [5] Kardjilov, N. et al. A highly adaptive detector system for high resolution neutron imaging. *Nucl. Instruments Methods Phys. Res. Sect. A Accel. Spectrometers, Detect. Assoc. Equip.* **651**, (2011).
- [6] Lehmann, E. H., Frei, G., Kühne, G. & Boillat, P. The micro-setup for neutron imaging: A major step forward to improve the spatial resolution. *Nucl. Instruments Methods Phys. Res. Sect. A Accel. Spectrometers, Detect. Assoc. Equip.* **576**, (2007).
- [7] Williams, S. H. et al. Detection system for microimaging with neutrons. *J. Instrum.* **7**, (2012).
- [8] Boillat, P. et al. In situ observation of the water distribution across a PEFC using high resolution neutron radiography. *Electrochem. commun.* **10**, (2008).
- [9] Krejci, F. et al. Development and characterization of high-resolution neutron pixel detectors based on Timepix read-out chips. *J. Instrum.* **11**, (2016).
- [10] Faenov, A. et al. Lithium fluoride crystal as a novel high dynamic neutron imaging detector with microns scale spatial resolution. *Phys. Status Solidi Curr. Top. Solid State Phys.* **9**, (2012).
- [11] Tremsin, A. S. et al. High resolution neutron imaging capabilities at BOA beamline at Paul Scherrer Institut. *Nucl. Instruments Methods Phys. Res. Sect. A Accel. Spectrometers, Detect. Assoc. Equip.* **784**, (2015).
- [12] Hussey, D. S., LaManna, J. M., Baltic, E. & Jacobson, D. L. Neutron imaging detector with 2 μm spatial resolution based on event reconstruction of neutron capture in gadolinium oxysulfide scintillators. *Nucl. Instruments Methods Phys. Res. Sect. A Accel. Spectrometers, Detect. Assoc. Equip.* (2017). doi:10.1016/j.nima.2017.05.035
- [13] Morgano, M. et al. Unlocking high spatial resolution in neutron imaging through an add-on fibre optics taper. *Opt. Express* **26**, (2018).
- [14] Trtik, P. et al. Improving the Spatial Resolution of Neutron Imaging at Paul Scherrer Institut - The Neutron Microscope Project. in *Physics Procedia* **69**, (2015).
- [15] Trtik, P. et al. Neutron Microtomography of MgB₂ Superconducting Multifilament Wire. in *Physics Procedia* **88**, (2017).
- [16] Trtik, P. & Lehmann, E. H. Isotopically-enriched gadolinium-157 oxysulfide scintillator screens for the high-resolution neutron imaging. *Nucl. Instruments Methods Phys. Res. Sect. A Accel. Spectrometers, Detect. Assoc. Equip.* **788**, (2015).
- [17] Trtik, P. & Lehmann, E. H. Progress in High-resolution Neutron Imaging at the Paul Scherrer Institut-The Neutron Microscope Project. *J. Phys. Conf. Ser.* **746**, (2016).
- [18] Grünzweig, C., Frei, G., Lehmann, E., Kühne, G. & David, C. Highly absorbing gadolinium test device to characterize the performance of neutron imaging detector systems. *Rev. Sci. Instrum.* **78**, (2007).
- [19] Trtik, P; Meyer, M; Wehmann, T; Tengattini, A; Atkins, D; Lehmann, E; Strobl, M. PSI 'Neutron Microscope' at ILL-D50 beamline - first results. *Mater. Research Forum* accepted for publication (2019).
- [20] Crha, J., Vila-Comamala, J., Lehmann, E., David, C. & Trtik, P. Light Yield Enhancement of 157-Gadolinium Oxysulfide Scintillator Screens for the High-Resolution Neutron Imaging. *MethodsX* **6**, 107–114 (2019).
- [21] Boillat, P. et al. Chasing quantitative biases in neutron imaging with scintillator-camera detectors: A practical method with black body grids. *Opt. Express* **26**, (2018).
- [22] Carminati, C. et al. Implementation and assessment of the black body bias correction in quantitative neutron imaging. *PLoS One* **14**, e0210300 (2019).
- [23] Kaestner, A. P. et al. The ICON beamline A facility for cold neutron imaging at SINQ. *Nucl. Instruments Methods Phys. Res. Sect. A Accel. Spectrometers, Detect. Assoc. Equip.* **659**, (2011).
- [24] Stuhr, U. Time-of-flight diffraction with multiple pulse overlap. Part I: The concept. *Nucl. Instruments Methods Phys. Res. Sect. A Accel. Spectrometers, Detect. Assoc. Equip.* **545**, 319–329 (2005).

- [25] Gong, W. et al. Hydrogen diffusion and precipitation in duplex zirconium nuclear fuel cladding quantified by high-resolution neutron imaging. *J. Nucl. Mater.* **526**, 151757 (2019).
- [26] Trtik, P. Neutron microtomography of voids in gold. *MethodsX* **4**, (2017).
- [27] Morgano, M., Peetermans, S., Lehmann, E. H., Panzner, T. & Filges, U. Neutron imaging options at the BOA beamline at Paul Scherrer Institut. *Nucl. Instruments Methods Phys. Res. Sect. A Accel. Spectrometers, Detect. Assoc. Equip.* **754**, 46–56 (2014).
- [28] Thimm, L; Trtik, P; Hansen, H; Jollet, S; Dinkelacker, F. Experimental cavitation and spray measurement in real-size nozzles with high-resolution neutron imaging. *ILASS 2019* (2019).
- [29] Liu, Q. et al. Gd₂O₂S:Tb scintillation ceramics fabricated from high sinterability nanopowders via hydrogen reduction. *Opt. Mater. (Amst)*. **94**, 299–304 (2019).
- [30] Hussey, D. S., LaManna, J. M., Baltic, E. & Jacobson, D. L. Neutron imaging detector with 2 μm spatial resolution based on event reconstruction of neutron capture in gadolinium oxysulfide scintillators. *Nucl. Instruments Methods Phys. Res. Sect. A Accel. Spectrometers, Detect. Assoc. Equip.* **866**, 9–12 (2017).
- [31] Mosconi, M. et al. Optical identification and quantification of single neutron detection in 6 LiF/ZnS scintillators using a CMOS camera. *J. Instrum.* **13**, P10033 (2018).
- [32] Wakonig, K. et al. X-ray Fourier ptychography. *Sci. Adv.* **5**, (2019).
- [33] Liu, D. et al. Demonstration of achromatic cold-neutron microscope utilizing axisymmetric focusing mirrors. *Appl. Phys. Lett.* **102**, (2013).
- [34] Boillat, P., Lehmann, E. H., Trtik, P. & Cochet, M. Neutron imaging of fuel cells – Recent trends and future prospects. *Curr. Opin. Electrochem.* **5**, (2017)

Announcements

The Name of the SGN/SNSS has changed to “Swiss Neutron Science Society”

The General Assembly of the Society on Nov. 26, 2018, has accepted to change the name of the Society from “Swiss Neutron Scattering Society” to the new name “Swiss Neutron Science Society”. This change of name reflects the openness of the SNSS for all researchers who need access to neutron sources. See the Minutes of the General Assembly in Swiss Neutron News 53 for more information.

SGN/SSDN Members

Presently the SGN/SSSN has 187 members. New members can register online on the SGN website: <http://sgn.web.psi.ch>

SGN/SSSN Annual Member Fee

The SGN/SSSN members are kindly asked to pay their annual member fee. At the general assembly 2013 of the society, the fee has been increased from CHF 10 to **CHF 20**. It can be paid either by bank transfer or in cash

during your next visit to the PSI. The bank account of the society is accessible for both Swiss national and international bank transfers: Postfinance: 50-70723-6 (BIC: POFICHBE), IBAN: CH39 0900 0000 5007 0723 6.

The SGN/SSSN is an organization with tax charitable status. All fees and donations paid to the SGN/SSSN are **tax deductible**.

PSI Facility News

Recent news and scientific highlights of the three major PSI user facilities SLS, SINQ and S μ S can be found in the **quarterly electronic newsletter** available online under: <https://www.psi.ch/science/facility-newsletter>

SINQ Upgrade

No neutrons are produced at the Swiss spallation neutron source SINQ in 2019, as SINQ receives a major upgrade in 2019 and 2020. The next call for beam-time proposals is planned to be launched early in 2020. Please visit the page <https://www.psi.ch/sinq/call-for-proposals> to obtain the latest information.

Registration of publications

Please remember to **register all publications either based on data taken at SINQ, SLS, SμS or having a PSI co-author** to the Digital Object Repository at PSI (DORA):

www.dora.lib4ri.ch/psi/

Please follow the link 'Add Publication'.

Open Positions at SINQ and ILL

To look for open positions at SINQ or ILL, have a look at the following webpages:

<https://www.psi.ch/pa/stellenangebote>

<https://www.ill.eu/careers/all-our-vacancies/?L=0>

PhD positions at ILL

The PhD program of the Institut Laue-Langevin, ILL, is open to researchers in Switzerland. Consult the page <https://www.ill.eu/science-technology/phd-students/home/> for information on the PhD program of ILL or get in contact with the managers of the program using the email address phd@ill.fr.

The Swiss agreement with the ILL includes that ILL funds and hosts one PhD student from Switzerland.

Conferences and Workshops 2019 and beyond

An updated list with online links can be found here:
<http://www.psi.ch/useroffice/conference-calendar>

November 2019

PSDI2019: 27th Protein Structure Determination in Industry meeting
November 3-5, 2019, Hinxtton,
United Kingdom

EMBO Course “Practical Integrative Structural Biology”
November 3-9, 2019, Hamburg, Germany

NoFuel-MMSNF 2019 Workshop
November 4-7, 2019, PSI Villigen, Switzerland

Cryo-EM Winter Workshop
November 5-7, 2019, Grenoble, France

First MicroED Workshop
November 6-8, 2019, Didcot,
United Kingdom

3D Imaging for Industry: Micro- and Nanotomography Symposium
November 7, 2019, Villigen, Switzerland

CATSA 2019: From Nanomaterial to Industrial Process
November 10-13, 2019, Langebaan,
South Africa

Artificial Intelligence Applied to Photon and Neutron Science
November 12-14, 2019, Grenoble, France

eBIC's 2019 Cryo-EM Sample Preparation Workshop
November 13-15, 2019, Didcot,
United Kingdom

AOCNS 2019: 3rd Asia-Oceania Conference on Neutron Scattering
November 16-21, 2019, Ken-Ting National Park, Taiwan

LEAPS Plenary Meeting 2019
November 18-20, 2019, PSI Villigen,
Switzerland

USTV SCHOOL ON THE CHARACTERIZATION
OF GLASS STRUCTURE

November 18-22, 2019, Grenoble, France

X-Rays and Matter

November 19-22, 2019, Villers-les-Nancy,
France

ADTB: Advanced Diffraction Techniques for
Biology

November 19-22, 2019, Grenoble, France

BCA Industrial and Chemical Groups meet-
ing “By hook or by crook – structural solu-
tions from challenging crystal”

November 20, 2019, Stevenage,
United Kingdom

GISAXS 2019

November 20-22, 2019, DESY Hamburg,
Germany

Dezember 2019

2019 MRS Fall Meeting

December 1-6, 2019, Boston, MA, USA

Symposium on Advanced Materials Explora-
tion with Neutrons at the Materials Re-
search Society (MRS) Fall Meeting 2019

December 1-6, 2019, Boston, MA, USA

Neutron Day and Farewell to BER II - Party

December 4, 2019, Berlin, Germany

Eleventh Joint BER II and BESSY II User
Meeting

December 4-6, 2019, Berlin, Germany

CONGA - Challenges and Opportunities of
New Generation Accelerator-based sources
December 9-10, 2019, Trieste, Italy

MLZ User Meeting 2019

December 10-11, 2019, Garching, Germany

FUSEE: FUTURE of SEEded free Electron lasers
December 10-11, 2019, Grignano
(near Trieste), Italy

BILL2019: Bilayers at the ILL - workshop
December 11-13, 2019, Grenoble, France

January 2020

SUM2020: 15th SOLEIL Users' Meeting
January 16-17, 2020, Synchrotron
SOLEIL, Gif-sur-Yvette, France

February 2020

Joint Polish-German Crystallographic Meet-
ing 2020

February 23-27, 2020, Wroclaw, Poland

March 2020

APS March Meeting 2020

March 2-6, 2020, Denver CO, USA

IFF spring school 2020

March 23 - April 3, 2020, Jülich, Germany

April 2020

Nanotech Singapore 2020
April 20-22, 2020, Singapore, Singapore

May 2020

LEAPS meets Quantum Technology
May 25-29, 2020, Elba, Italy

June 2020

Bombannes 2020: 15th Bombannes Summer School on Scattering Methods Applied to Soft Condensed Matter
June 16-24, 2020, Bombannes/Carcans-Maubuisson, Gironde, France

July 2020

11th Liquid Matter Conference 2020
July 20-24, 2020, Prague, Czech Republic

September 2020

PSI Power diffraction school
September 13-18, 2020, PSI Villigen, Switzerland

July 2021

ICNS: International Conference on Neutron Scattering 2021
July 4-8, 2021, Argentina

Editorial

Editor

Swiss Neutron Science Society

Board for the Period 2019 – 2021:

President

Prof. Dr. H. Ronnow
henrik.ronnow@epfl.ch

Board Members

Prof. Dr. M. Strobl
markus.strobl@psi.ch

PD Dr. K. Krämer
karl.kraemer@dcb.unibe.ch

PD Dr. U. Gasser (secretary)
urs.gasser@psi.ch

Honorary Members

Prof. Dr. W. Hälg, ETH Zürich (†)

Prof. Dr. K. A. Müller
IBM Rüschlikon and Univ. Zürich

Prof. Dr. A. Furrer
ETH Zürich and Paul Scherrer Institut

Auditors

Dr. M. Zolliker, Paul Scherrer Institut
Prof. Dr. Florian Piegsa, Univ. Bern

Address

Sekretariat SGN/SSSN
c/o Paul Scherrer Institut
WLGA/018
5232 Villigen PSI, Switzerland
phone: +41 56 310 46 66
fax: +41 56 310 32 94
<http://sgn.web.psi.ch>

Bank Account

Postfinance: 50-70723-6 (BIC: POFICHBE)
IBAN: CH39 0900 0000 5007 0723 6

Printing

Paul Scherrer Institut
Circulation: 1600
2 numbers per year

Copyright

SGN/SSSN and the respective authors

Swiss Neutron Science Society

Sekretariat SGN/SSSN
WLGA/018
Paul Scherrer Institut
5232 Villigen PSI, Switzerland

